IEEE Photonics Journal
An IEEE Photonics Society Publication

Open Access

Dipole-Based Wavelet Superposition for Accurate Design and Analysis of Metasurface

Volume 12, Number 5, October 2020

Hongjun Chu
Jiaran Qi
Jinghui Qiu

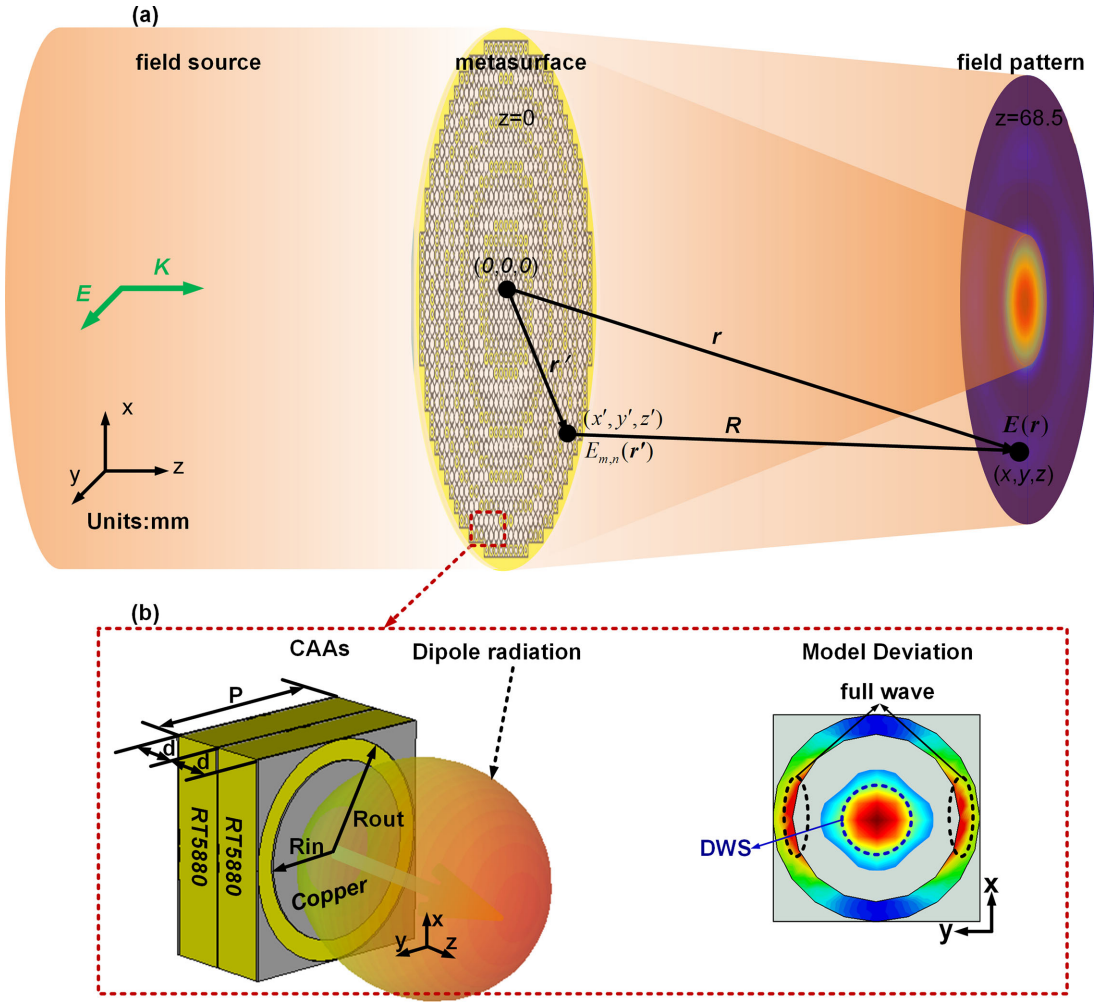

DOI: 10.1109/JPHOT.2020.3029123

Dipole-Based Wavelet Superposition for Accurate Design and Analysis of Metasurface

Hongjun Chu, Jiaran Qi, and Jinghui Qiu

Department of Microwave Engineering, Harbin Institute of Technology, Harbin 150001, China

DOI:10.1109/JPHOT.2020.3029123

Manuscript received June 10, 2020; revised September 29, 2020; accepted October 2, 2020. Date of publication October 7, 2020; date of current version October 15, 2020. This work was supported by the National Natural Science Foundation of China under Grants 61671178, 61731007, and 61301013. Corresponding authors: Jiaran Qi; Jinghui Qiu (e-mail: qi.jiaran@hit.edu.cn; qiujh@hit.edu.cn).

Abstract: Design and analysis of metasurface-based devices mainly rely on the ideal ray theory and full-wave simulation technique. However, for near-field and low-frequency applications, these idealized design and time-consuming full-wave simulation methods often suffer from inaccuracy and inefficiency, which hinders the rapid prototyping and further evolution of metasurface-based devices. Here, dipole-based wavelet superposition (DWS) is proposed and formulated to accurately and efficiently design the metasurface and analyze its diffraction field, by treating unit cell on the metasurface and every wavefront representing the target field as Hertzian dipole. We further define quantitatively an effective zone, within which the proposed DWS offers sufficiently accurate results comparable to the full-wave simulation. A series of numerical experiments on design and analysis of metasurface are then carried out to validate our DWS method. Excellent and more superior consistence with the full-wave analysis and theoretical results confirms that the DWS method provides an advanced closed-loop design and analysis tool with significantly improved accuracy and efficiency for metasurface-based devices.

Index Terms: Metasurfaces, metasurface design and analysis, dipole-based wavelet superposition, paraxial and non-paraxial, near-field and far-field, effective computational zone.

1. Introduction

In recent years, various metasurface-based devices featuring small cubage, multi-functionality, superior capability, high dependability, and ease of integration, have received continuously growing attention [1]–[6]. A typical design flow of a metasurface involves rigorous full-wave simulation followed by conversion of the desired phase profile into a metasurface Graphic Database System II (GDSII) layout for fabrication purposes [7]. To be more specific, implementing a metasurface device can be divided into five main parts, namely: (1) modeling unit cell to achieve 0-2π phase coverage at the frequency band of interest, (2) generating the phase profile of the desired metasurface device, (3) converting the phase profile into a metasurface GDSII layout, (4) modeling the metasurface GDSII layout and validating the design by performing numerical analysis on the metasurface, (5) fabrication. In the design process of the metasurface, steps (2) and (4) involve two core issues: generating inversely the desired phase profile (metasurface design) and analyzing forwardly the diffracted field distribution by the generated metasurface layout (metasurface analysis). In essence,

it involves two field computation problems, one is to compute the phase profile on the metasurface according to the desired target field, and the other is to calculate the diffraction field generated by the metasurface.

For the design of versatile metasurfaces such as focusing lenses, holographic interference recorder, and waveplates, geometric optics, diffraction theory, and their variants [8]–[14], are most frequently adopted to generate the desired phase profile. These methods are essentially the ray theory or simplified wave theory, where simplifying assumptions are made, e.g., electromagnetic (EM) waves are modeled as geometric rays, desired target fields are discretized into a set of ideal point sources, and some EM effects such as diffraction and interference are ignored. These assumptions will generate non-negligible errors for near-field or non-optical low-frequency applications, where significant diffraction effect might occur, and these methods are thus expected to lose the prediction power. As for the metasurface analysis, that is, to compute the diffraction field generated by a metasurface, the typically adopted full-wave simulation is often time-consuming. It will greatly reduce the design efficiency of metasurface and also make impossible its cooperation with iterative optimization. To address this issue, Huygens-Fresnel principle (HF) and its variants have been adopted, where the diffraction wavefront is interpreted as the superposition of spherical wavelets radiating by fictitious infinitesimal point sources on the diffraction aperture (i.e., metasurface). They have been successfully applied to accurately estimate the far-field patterns diffracted by the metasurface [15]–[19], but failed to compute its diffraction field within the near-field region including the evanescent area with acceptable accuracy. As aforementioned, in these near-field regions many advanced applications have emerged, such as large field-of-view near-field imaging [20], [21], planar and stereo holography [22], [23], near-field ptychography [24], and immersion interference photolithography [25], [26]. Therefore, how to rapidly yet accurately estimate the diffraction near-field and far-field generated by the metasurface and reversely the phase profile on the metasurface according to the desired target field thus becomes an issue of practical significance.

To tackle these issues, inspired by the Helmholtz-Kirchhoff diffraction integral theory and its pattern-propagation Eigenfactor [27], we adopt Hertzian dipole instead of point source to model the subwavelength unit cell on the metasurface and every wavefront representing the target field. According to the theory of wave propagation theory and the superposition theorem of the field, dipole-based wavelet superposition (DWS) is then formulated to fulfill the computations. We further define quantitatively an effective computational zone, within which the proposed DWS offers sufficiently accurate results comparable to the full-wave simulation. On one hand, to demonstrate its superiority in calculating the diffraction-field generated by metasurface, we set up a series of numerical experiments involving the subwavelength unit cell, on-axis near/far-field focusing metasurfaces, and off-axis near/far-field focusing metasurfaces, respectively. Their diffraction field patterns are calculated by the DWS, and compared with those extracted by the finite-different time-domain (FDTD) full-wave analysis, Huygens-Fresnel principle (HF), and Huygens' Principle (HP). On the other hand, to verify its validity and accuracy in the metasurface design, complex amplitude holographic metasurfaces are constructed by the DWS to generate the scaled-down Big Dipper flat pattern inside and outside the near-field zone. Their holographic field patterns are compared with the theoretical ones and those generated by the holographic metasurfaces designed by the point-source-based wavelet superposition (PSWS, i.e., HP). Finally, concluding remarks are given. It is noted that in this paper these illustrative experiments are set up at millimeter-wave band, where the aperture of the metasurface-based device is quite limited due to the dimension and the strength constrains of available materials. However, the proposed method is applicable to the entire electromagnetic spectrum.

2. Modeling and Formulation of Dipole-Based Wavelet Superposition

In the theory of wave propagation and the superposition theorem of the field, a new diffraction or interference wavefront can be interpreted as a constructive or destructive superposition of wavelets generating from an infinity of fictitious 'secondary' point sources in the primary wavefront. Such

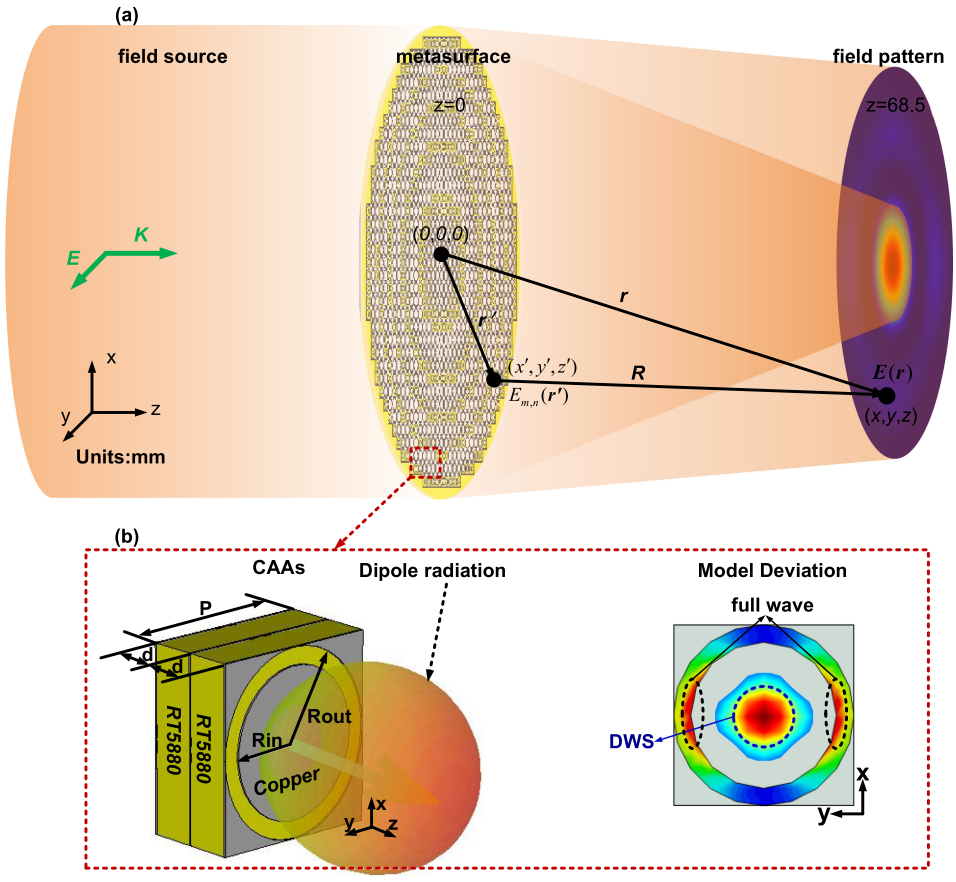

Fig. 1. The 2D metasurface schematic diagram for formulating the DWS in the Cartesian coordinate system. (a) An illustrative focusing metasurface of numerical aperture (NA) of 0.55 and focal distance (*fd*) of 76 mm under normal illumination of a *y*-polarized Gaussian plane-wave at 35 GHz and its electric-field-intensity pattern on the $z = 68.5$ mm plane computed by the DWS (almost same results can be obtained by the HF and the HP). (b) The unit cell (coaxial annular apertures (CAAs) [10]) and its equivalent dipole radiation model along with its model deviation in the red dotted box are zoomed and also inserted in the figure.

a principle in EM wave has been mathematically derived from Helmholtz equation and Green's theorem and further formulated into an integral theorem of Helmholtz and Kirchhoff, which can be rigorously derived from Maxwell's equations [28], [29]. Huygens' Principle, Huygens-Fresnel principle, and their variants are the outgrowth of this integral theorem. According to this principle, when each point of the reference wavefront is modeled as a dipole source rather than a point source and spreads outward, the diffraction fields can be thus expressed as the interference and superposition of fields generated by the oscillating dipoles. As for the two-dimensional (2D) metasurface, its diffraction field patterns can be also represented in a similar way, when its building block, i.e., unit cell, is regarded as an equivalent dipole. It is noted that the equivalent dipole model of unit cells has been generally accepted in many reports [29]–[32].

Here, we take metasurface as the example to formulate dipole-based wavelet superposition (DWS). To facilitate the analysis and without loss of generality, assuming that the incident plane wave is linearly polarized in the *y*-direction, the metasurface is located on the $z = 0$ plane and is a zero-thickness isotropic grid sheet assembled by geometrically different unit cells, as exhibited in Fig. 1(a). As shown in the red dotted box of Fig. 1(b), unit cell is modeled as a forward Hertzian dipole located at its centre, whose amplitude, phase, and polarization are determined by its own

structure and material properties as well as the incident wave. Then, the diffraction electric-field at any observation point $\boldsymbol{r}$, $E(\boldsymbol{r})$, superposed by wavelets generated from all excited dipoles (unit cells), can be represented as,

$$E(\mathbf{r}) = \sum_{m,n} E_{m,n}(\mathbf{r}') \left[\frac{S_{cell}}{2\pi} \left(1 + j\frac{1}{kR} + j\frac{1}{k^2R^2} \right) \sin(\mathbf{e}_x, \mathbf{R}) \frac{-jke^{jkR}}{R} \right]. \tag{1}$$

where $E_{m,n}(\boldsymbol{r}')$ is the complex amplitude of dipole associated with the incident wave and the mth row nth column unit cell on the metasurface, k is the wave number corresponding to the wavelength λ, $\boldsymbol{R} = \boldsymbol{r}\text{-}\boldsymbol{r}'$ with its module value of $R = |\boldsymbol{r}\text{-}\boldsymbol{r}'|$ is the distance vector from the source point $\boldsymbol{r}'$ to the observation point $\boldsymbol{r}$, $\boldsymbol{r}$ and $\boldsymbol{r}'$ are the distance vectors from the origin point (*0*, *0*, *0*) to the observation point (x, y, z) and the source point (x', y', z'), and $\boldsymbol{e}_x$ is the unit vector in the x-direction. S_{cell} is the cross sectional area of the unit cell. Note that $1/(2\pi)$ is introduced into the Eq. (1) in order to keep uniform with Huygens's Principle, Huygens-Fresnel principle, and their variants.

As $E(\boldsymbol{r})$ expressed in Eq. (1), the diffraction field at the observation point $\boldsymbol{r}$ can be regarded as the constructive or destructive superposition of wavelets generated from all unit cells on the metasurface. Here, we term this method as dipole-based wavelet superposition (DWS). From Eq. (1), the DWS is a high-efficient diffraction field calculation method with low time complexity. Assuming a metasurface is composed of M unit-cells, its diffraction field at any observation point $\boldsymbol{r}$ only involves M complex multiplications. Then, if the diffraction field on the target plane has L pixel numbers (observation points), the total time complexity of the DWS requires $L\times M$ complex multiplications. That is, the time complexity of the DWS depends on the unit-cell number on the metasurface and the pixel number on the target plane. As an experimental verification, the diffraction pattern with every pixel pitch of 1×1mm^2 on the target plane of 80×80 mm^2 generated by a focusing metasurface with 2269 meta-atoms is numerically calculated by using the DWS in MATLAB. The computer configuration is as follows: Intel(R) Core(TM) i5-6200u CPU@2.3GHz, 4G RAM, and 64-bit OS. The whole process from modeling metasurface to calculating its diffraction field takes 1min 36s.

In this way, if each unit cell on the metasurface is modeled to be different types of oscillation sources, e.g., point source, dipole, or their combination, different forms of diffraction field expressions can be thus derived easily from their wavelet superpositions. Similarly, every wavefront on the target field is modeled as the oscillating dipole, and the diffraction field at the metasurface generated by the target field can be also deduced by using the DWS. Here, to facilitate understanding this process, assume that the target field is distributed over an imaginary aperture.

For comparison purposes, we provide the formula of the PSWS similar to the DWS, which reads,

$$E(\mathbf{r}) = \sum_{m,n} E_{m,n}(\mathbf{r}') \frac{S_{cell}}{2\pi} \frac{-jke^{jkR}}{R}. \tag{2}$$

Obviously, when the observation region is located at the paraxial far-field zone of metasurface or imaginary aperture, the higher-order term $1/R^2$, $1/R^3$ can be ignored and $\sin(\boldsymbol{e}_x, \boldsymbol{R}) \approx 1$ in Eq. (1). Eq. (1) can thus be approximately reduced to Eq. (2). However, when the observation region is located within the near-field or non-paraxial region of metasurface or imaginary aperture, the diffraction field calculated by the DWS is very different from that extracted by the PSWS in both amplitude and phase.

Here, it should be emphasized that for any unit cell in their infinite periodic array, the actual resonance may occur at its any part, which is determined by its specific structure and the incident wave involving frequency, polarization, and propagation direction. As shown in Fig. 1(b), under a y-polarized Gaussian plane-wave illumination, the internal annular grooves of CAAs along the direction of polarization (black elliptic dotted line) are excited and generate resonances. However, when modeling unit cell by a dipole, its geometrical centre is set to be the oscillation source, as exhibited by the blue circular dotted line in Fig. 1(b). Obviously, this modeling deviation in turn causes calculation error in estimating the field modulated by unit cell, especially within its deep subwavelength near-field region. To weaken this modeling deviation and its impact, the difference

between the distance from the observation point (x, y, z) to the actual resonance point and that to the modeling centre should satisfy the following equation, which reads,

$$\left|\sqrt{\rho'^2+z^2}-\sqrt{\rho^2+z^2}\right| \le \min(\sqrt{\rho'^2+z^2}, \sqrt{\rho^2+z^2})\Big/N. \tag{3}$$

where $\rho' = \sqrt{(x-x'')^2+(y-y'')^2}$, $\rho = \sqrt{(x-x')^2+(y-y')^2}$, and N is an arbitrary constant.

For an infinite periodic unit cell array, within its orthographic projection region concerned, Eq. (3) can be converted to the following inequality, which is expressed as,

$$\sqrt{P^2/2+z^2}-z \le z/N. \tag{4}$$

Here, in order to ensure that this difference is small enough, N is set to 10 in this paper. For $N = 10$, that means $z \ge 1.54$P, where P is the lattice period of unit cell. Therefore, to minimize this deviation, the observation point should be moved beyond 1.54P away from unit cell, so that the distance vector from the observation point to any part of unit cell is almost the same. A characteristic threshold, i.e., 1.54P, is thus defined to enable the effective computation of the DWS. In this case, the higher-order term $1/R^3$ in Eq. (1) can be ignored, and the diffraction field $E(\boldsymbol{r})$ based on DWS can be thus simplified as,

$$E(\mathbf{r}) = \sum_{m,n} E_{m,n}(\mathbf{r}')\left[\frac{S_{cell}}{2\pi}\left(1+j\frac{1}{kR}\right)\sin(\mathbf{e}_x, \mathbf{R})\frac{-jke^{jkR}}{R}\right]. \tag{5}$$

As discussed above, the DWS evidently shows that the diffraction field generated by metasurface, $E(\boldsymbol{r})$, may be described as the interference field at (x, y, z) arising from wavelets generated from all unit cells on the metasurface. Furthermore, when $1/(kR) = 0.1<<1$, i.e., $R = 10/k$, the $1/(kR)$ and its high-order term $1/(k^2R^2)$ in Eq. (1) and Eq. (5) can be ignored, and within the paraxial region Eq. (1) and Eq. (5) are consistent with Eq. (2) in form. This means that within the paraxial far-field region of the metasurface the DWS is unified with Huygens' Principle.

3. Numerical Experiments on the Metasurface Diffraction Field Estimation

Let us first consider the metasurface diffraction field calculation. A subwavelength unit cell in their infinite periodic array is firstly modeled and characterized by the DWS in this section. Here, we arbitrarily select the CAAs as an illustrative case, whose geometrical details are shown in Fig. 1(b). The amplitude and phase patterns of the diffraction field within three adjacent regions are computed by the DWS and compared with those extracted by the FDTD full-wave solver, the HF, and the HP. As the second example, under normal illumination by a y-polarized Gaussian plane-wave at 35 GHz, four representative on-axis and off-axis, paraxial and non-paraxial focusing metasurfaces with the same apertures of 54 mm are designed by the geometrical optics (i.e., the PSWS) and assembled by geometrically different CAAs, respectively. Their focal spots are set at (0, 0, 5), (0, 0, 20), (10, 0, 5), and (30, 0, 15), respectively. Similar computation and comparison are performed. It is noted that the CAAs (as shown in figure 1) show excellent EM properties, such as high transmission coefficients (more than 0.85), full 2π phase coverage, wide-angle stability (more than 30 degrees), and polarization-independence [10].

3.1 The Subwavelength CAAs of $R_{in} = 1.21$ mm

As shown in Fig. 2, we divide the computational region into three adjacent intervals, i.e., region I: $0 \le z \le 1.54$P (lattice period P = 3 mm), region II: $1.54\text{P} \le z \le 10/k$, and region III: $10/k \le z \le 10/k + 20$. For region I, from Fig. 2 the axial normalized amplitude and phase patterns on the $x = 0$ plane indicate that there exist significant differences among the FDTD full-wave simulation results and the numerical calculation ones extracted by the DWS, the HF, and the HP, as might have been expected by the theoretical analysis above. It is mainly attributed to the distance vector deviation between the real resonance positions and the modeled one, as well as the calculation

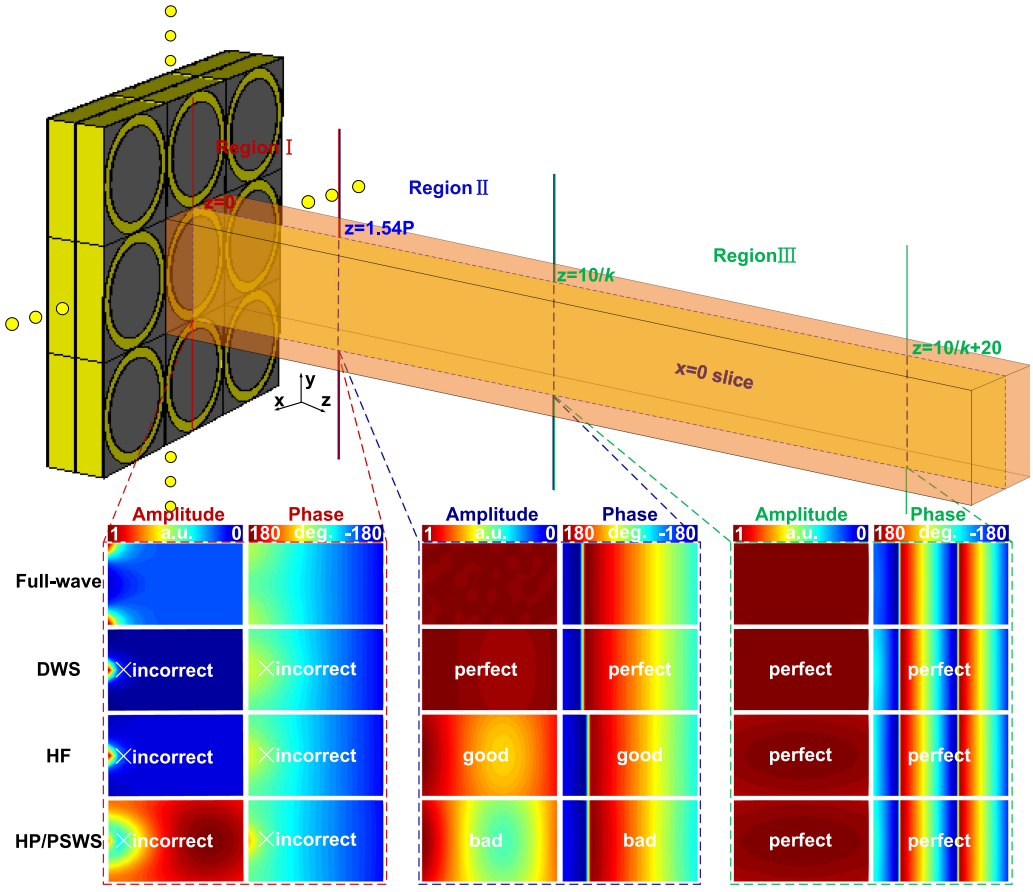

Fig. 2. The axial normalized amplitude and phase patterns on the $x = 0$ plane within the region I, the region II, and the region III, modulated by the subwavelength CAAs of $R_{in} = 1.21$ mm under a *y*-polarized Gaussian Plane-wave excitation, which are extracted by the FDTD full-wave solver, the DWS, the HF, and the HP/PSWS, respectively. It should be noted that $10/k$ as the zoning boundary is given in section 2. As for another zoning boundary, $10/k + 20$ is set arbitrarily to illustrate our discussing problem. If necessary, it can be$10/k + 30$, $10/k + 40$, or more.

methods themselves ignoring the weak coupling among unit cells. In region II, the distance from the observation point to any part of unit cell surface is almost the same so that the effect of resonance position deviation can be ignored. As exhibited in Fig. 2, it is shown that within region II the DWS provides satisfactory agreement with the full-wave analysis both in amplitude and phase patterns. However, the HF and the HP show bad accuracy in estimating the diffraction field. When the distance from the observation point to unit cell gradually increases beyond $10/k$, the differences among the above numerical methods rapidly diminish especially within the paraxial far-field region of $\sin(\boldsymbol{e}_x, \boldsymbol{R}) \approx 1$, as intuitively indicated by their amplitude and phase patterns within region III in Fig. 2. In general, it is demonstrated that compared to point source, dipole can inherently characterize the EM scattering properties of unit cell. Furthermore, when the observation region is beyond the characteristic threshold, i.e., 1.54P, the DWS can be enabled to accurately calculate the metasurface diffraction field.

3.2 The On-Axis and Off-Axis Focusing Metasurfaces

Firstly, an on-axis focusing metasurface with its focal spot set at (0, 0, 5) is constructed. As shown in Fig. 3(a), within the subwavelength near-field paraxial region, the axial and radial normalized

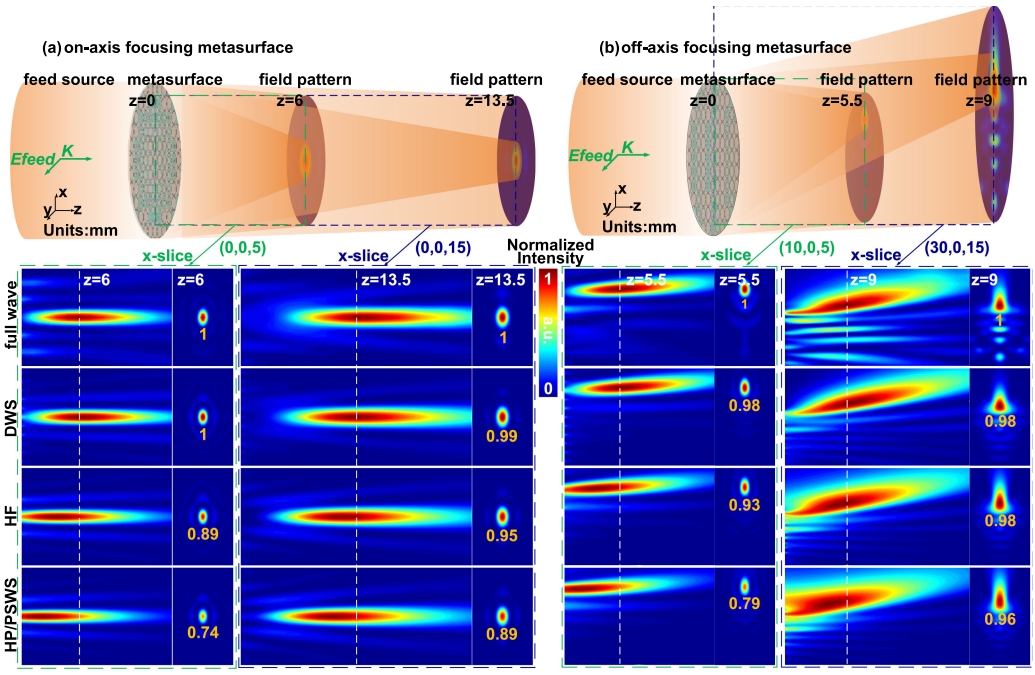

Fig. 3. The on-axis and off-axis focusing schematic diagram and the simulated and calculated normalized intensity patterns generated by the on-axis and off-axis focusing metasurfaces. (a) for the on-axis near-field and far-field focusing metasurfaces, and (b) for the off-axis near-field and far-field focusing metasurfaces. The brown numbers represent the maximum normalized intensities within the observation plane.

TABLE 1
The Focusing Parameters Characterizing the On-Axis Focal Beam Quality and Shape (Unit: mm)

Parameter		*Focus*	*DOF*	*FWHMx/FWHMy*	*Max.* (a.u.)
Near-field	FDTD	(0, 0, 6)	9.5	3.9/3.9	1
	DWS	(0, 0, 6)	9.6	3.8/3.8	1
	HF	(0, 0, 4)	9.8	3.7/3.7	0.89
	HP/PSWS	(0, 0, 2.5)	8.3	3.6/3.6	0.74
Far-field	FDTD	(0, 0, 13.5)	16.1	5.0/5.3	1
	DWS	(0, 0, 13)	16.1	5.1/5.1	0.99
	HF	(0, 0, 11.5)	15.3	4.9/4.9	0.95
	HP/PSWS	(0, 0, 10.5)	14.6	4.8/4.8	0.89

intensity patterns on the $y = 0$ and $z = 6$ mm (2P) plane computed by the DWS, both show excellent agreement with the FDTD full-wave simulation ones. Furthermore, the focusing parameters characterizing the focal beam quality and shape, such as the focus position (*Focus*), maximum normalized intensity (*Max.*) on the focal plane, the axial depth of focus (*DOF*), radial full width at half maximum in the *x*-direction (*FWHMx*) and in the *y*-direction (*FWHMy*), are almost perfectly matched with each other, as listed in Table 1. However, significant differences between the intensity patterns computed by the HF/HP and those extracted by the FDTD full-wave solver can be clearly observed, showing quite inconsistent focal positions, distinctly different focal beam shapes, and large intensity deviations. When the focal spot (0, 0, 20) is moved to the far-field zone, similar phenomena and conclusions can be observed and obtained, as shown in Fig. 3(a) and Table 1. Compared to the near-field focusing case, the far-field focusing results show that the differences among them decrease significantly. When the region of interest is far away from the evanescent region, it means that the near-field factor $1/kR$ is much less than 1 and $\sin(\boldsymbol{e}_x, \boldsymbol{R})$ gets closer to 1.

TABLE 2
The Focusing Parameters Characterizing the Off-Axis Focal Beam Quality and Shape (Unit: mm)

Parameter		*Focus*	*DOF*	*FWHMx/FWHMy*	*Max.* (a.u.)
Near-field	FDTD	(9.5, 0, 5.5)	8.3	4.4/4.1	1
	DWS	(10, 0, 6)	8.5	4.4/3.9	0.98
	HF	(9.5, 0, 3.5)	8.7	4.3/3.8	0.93
	HP/PSWS	(9.5, 0, 2.5)	6.7	4.3/3.7	0.79
Far-field	FDTD	(19.5, 0, 9)	9.9	11.4/6.6	1
	DWS	(20, 0, 9.5)	10.2	10.8/7.4	0.98
	HF	(20, 0, 8)	11.2	14.2/6.4	0.98
	HP/PSWS	(20, 0, 7)	13.0	16.0/6.4	0.96

In this case, the three methods have almost the same integral formulas and thus show consistent calculation results. In general, the field distributions together with the focusing parameters both confirm that compared to the HF and the HP, the DWS can more accurately estimate the paraxial near-field patterns generated by the metasurface, exhibiting perfect agreement with the FDTD full-wave analysis. It is noted that the $z = 6$ mm (2P) and $z = 13.5$ mm (4.5P) plane are the focal planes of the on-axis near-field and far-field focusing metasurfaces, respectively, which are determined by the FDTD full-wave solver.

For the off-axis near-field focusing case, within the non-paraxial near-field region, similar phenomenon can be also observed in Fig. 3(b). The axial and radial intensity patterns on the $y = 0$ plane and $z = 5.5$ mm (1.83P) plane distinctly indicate that the DWS provides better consistency with the FDTD full-wave analysis than the HF and the HP. The focusing parameters characterizing the focal beam quality and shape, which are calculated and listed in Table 2, also confirm this point. When the focal spot is set at (30, 0, 15) in the non-paraxial far-field zone, the normalized intensity patterns in Fig. 3(b) and the focusing parameters in Table. 2 both show the DWS firmly present superior capability in estimating the metasurface diffraction field. Large differences exist between the full-wave analysis and the point-source-based HP/PSWS. The off-axis focusing metasurface again exemplifies that the DWS can estimate the non-paraxial diffraction field patterns with higher accuracy than the HF and the HP, and provide excellent agreement with the full-wave analysis. Likewise, the $z = 5.5$ mm (1.83P) and $z = 9$ mm (3P) planes are the focal plane of the off-axis near-field and far-field focusing metasurfaces, respectively, which are determined by the FDTD full-wave solver.

In general, the above series of illustrative examples show that the DWS can accurately estimate the metasurface diffraction field patterns within the paraxial and non-paraxial near-field and far-field region, and provide better and satisfactory agreement with the FDTD full-wave analysis than the HF and the HP. It implies that the wavelet superposition based on oscillating dipole can more accurately model the subwavelength unit cell and characterize the metasurface diffraction field than the point-source-based wavelet superposition.

4. Numerical Experiments on the Metasurface Design

As proved above, the DWS shows satisfactory superiority in accurately computing the metasurface diffraction field, and exhibits perfect agreement with the full-wave analysis. Next, we investigate and evaluate its capacity in deducing the required field at the metasurface from the target field for generating the desired phase profile. Here, to test its validity and accuracy, we carefully set up two complex amplitude holographic metasurfaces. They are designed by using the DWS and the PSWS to generate the same Big Dipper flat pattern within the near-field and far-field region, respectively. The Big Dipper is composed of seven bright stars, i.e., Dubhe, Merak, Phecda, Megrez, Alioth, Mizar, and Alkaid, whose brightness are roughly normalized to 1, 1, 1, 0.65, 1, 1, and 1 according to the apparent magnitude, respectively. According to their relative positions in space, the seven stars are modeled to be seven bright spots on some radial plane as shown in Fig. 4. For both the near-field and far-field cases, the seven bright spots are placed at (−30, 16, 5), (−16, 12, 5), (−10,

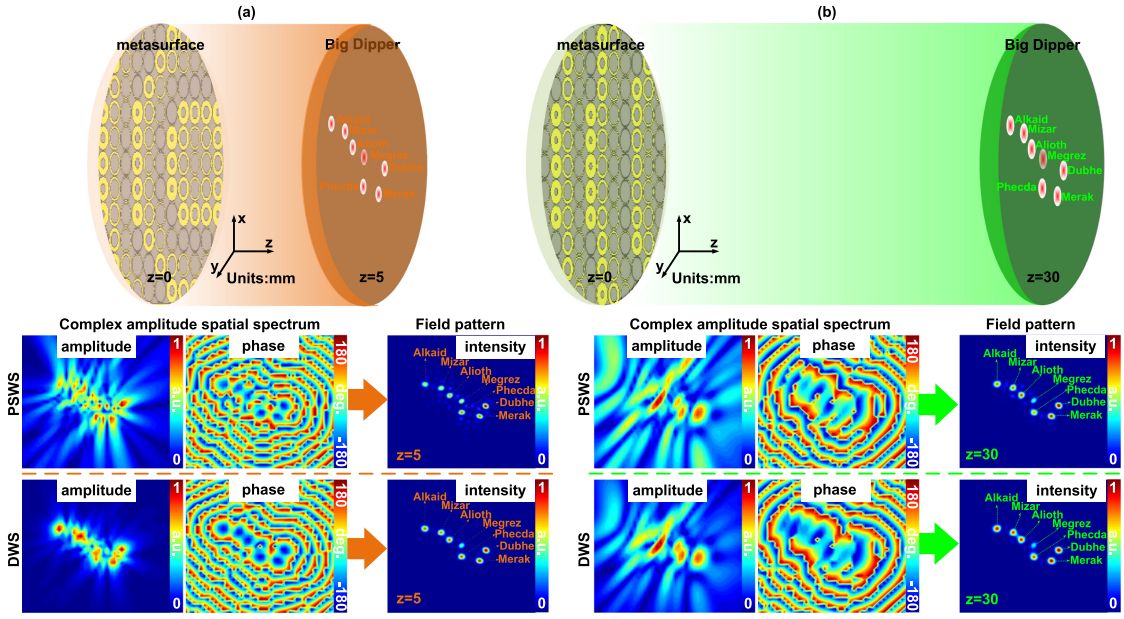

Fig. 4. The normalized amplitude and phase patterns on the holographic metasurfaces ($z = 0$ plane) calculated by the PSWS and the DWS, respectively, and their Big Dipper holographic field patterns on the $z = 5$ mm and $z = 30$ mm plane extracted by the DWS. (a) for the near-field Big Dipper holographic pattern, (b) for the far-field Big Dipper holographic pattern.

6, 5), (0, 0, 5), (0, −9, 5), (15, −13, 5), (−20, 4, 5) on the $z = 5$ mm (1.67P) plane and (−30, 16, 30), (−16, 12, 30), (−10, 6, 30), (0, 0, 30), (0, −9, 30), (15, −13, 30), (−20, 4, 30) on the $z = 30$ mm (10P) plane, respectively. Then, the required fields at the metasurface ($z = 0$ plane) generated by the seven bright spots can be derived by the DWS and the PSWS, respectively. The complex amplitude holographic metasurfaces can be further assembled by geometrically different unit cells to approximately generate the required complex amplitude profiles. It should be noted that when discretely quantifying and rebuilding the desired complex amplitude profiles, the quantification itself and the non-ideal unit cells both inevitably introduce the indeterminate errors. Furthermore, due to mutational EM boundary conditions among the geometrically different unit cells on the practical metasurface, it will result in uncertain phase jump and amplitude change of the unit cell. It, in turn, will lead to the unpredictable uncertainty amplitude and phase distributions generated by the designed metasurface. Therefore, to study and evaluate the performance of the design or calculation methods themselves, these uncontrollable factors should be avoided. In this paper the complex amplitude profiles on the metasurface computed by the DWS and the PSWS are directly extracted to be the amplitudes and phases of the 'fictitious' subwavelength unit cells to construct the 'fictitious' complex amplitude holographic metasurfaces. Meanwhile, their holographic field patterns are computed by the DWS. It is noted that the two holographic metasurfaces still operate at 35 GHz and have the same aperture of 120 mm. The lattice period of the 'fictitious' unit cells is still P = 3 mm.

Firstly, the near-field holography is considered. The amplitude and phase patterns at the metasurface are derived by the PSWS and DWS from the target Big Dipper patterned field on the $z = 5$ mm (1.67P) plane, respectively. Obviously, there exist big differences between them in both amplitude and phase, as exhibited in Fig. 4(a). The maximum amplitude difference is up to 0.39, and the phase differences are mainly around 40 degrees. Intuitively, as shown in Fig. 4(a), the Big Dipper holographic field pattern generated by the metasurface designed by the DWS is closer to the target one, and quite different from that generated by the metasurface designed by the PSWS. The intuitive result is further confirmed by the statistical data about the positions of the seven

TABLE 3
The Positions of the Seven Bright Specks and Their Relative Amplitudes for the Near-Field Case (Unit: mm)

Big Dipper	Target field pattern (coordinate)---amplitude	Near-field pattern (coordinate)---amplitude	
		DWS	PSWS
Dubhe	(20, -4, 5)---1	(20, -4, 5)---1	(19.5, -4.5, 5)---1
Merak	(15, -13, 5)---1	(15, -13, 5)---0.94	(15, -13, 5)---0.89
Phecda	(0, -9, 5)---1	(0, -9.5, 5)---0.91	(0, -9.5, 5)---0.90
Megrez	(0, 0, 5)---0.65	(0, 0.5, 5)---0.71	(0, 0.5, 5)---0.82
Alioth	(-10, 6, 5)---1	(-9.5, 6, 5)---0.90	(-9.5, 5.5, 5)---0.86
Mizar	(-16, 12, 5)---1	(-16.5, 12.5, 5)---0.88	(-16.5, 12.5, 5)---0.82
Alkaid	(-30, 16, 5)---1	(-29.5, 16, 5)---0.91	(-29.5, 16, 5)---0.78

TABLE 4
The Positions of the Seven Bright Specks and Their Relative Amplitudes for the Far-Field Case (Unit: mm)

Big Dipper	Target field pattern (coordinate)---amplitude	Far-field pattern (coordinate)---amplitude	
		DWS	PSWS
Dubhe	(20, -4, 30)---1	(20.5, -3.5, 30)---1	(20.5, -3.5, 30)---1
Merak	(15, -13, 30)---1	(14.5, -13.5, 30)---0.98	(14.5, -13, 30)---0.95
Phecda	(0, -9, 30)---1	(0.5, -10, 30)---0.90	(0.5, -10, 30)---0.87
Megrez	(0, 0, 30)---0.65	(0, 1, 30)---0.63	(0, 1, 30)---0.68
Alioth	(-10, 6, 30)---1	(-10, 6, 30)---0.93	(-10, 6, 30)---0.91
Mizar	(-16, 12, 30)---1	(-16.5, 12.5, 30)---0.93	(-17, 12.5, 30)---0.90
Alkaid	(-30, 16, 30)---1	(-29.5, 16, 30)---0.95	(-29.5, 16, 30)---0.89

bright specks and their relative amplitudes, as listed in Table 3. It is demonstrated that compared to the PSWS, the DWS can capture the amplitude and phase information of the target field more accurately, and in turn facilitate the accurate design of various metasurface-based devices. It is also indicated that the dipole is more reasonable to model every wavefront on the target field than the point source.

For the far-field holography case, similar computation and comparison are conducted as well. As shown in Fig. 4(b), when the holographic metasurface is moved away from the target plane, the differences between the amplitude (phase) patterns computed by the PSWS and DWS get smaller, just as their formulas inherently imply. The maximum amplitude difference is reduced to 0.19, and the phase differences mainly keep around 15 degrees. The generated Big Dipper field patterns are both very close to the target one, which is further confirmed by their coordinates and relative amplitudes in Table 4. The amplitude-phase holographic metasurface designed by the DWS generates a better Big Dipper pattern on the specified plane, which is almost the same as the target one. Again, it is demonstrated that the DWS can accurately and effectively estimate the desired complex amplitude profile and in turn synthesize the metasurface layout.

5. Conclusion

In conclusion, in this paper the DWS as a superior metasurface design and analysis tool is first formulated by modeling the subwavelength unit cell on the metasurface and every wavefront on the target field as Hertzian dipole. A quantified characteristic threshold, i.e., 1.54P, is defined to enable the validity and accuracy of the proposed DWS in calculating the diffraction field generated by the metasurface and the target field. A series of all-embracing numerical experiments are set up and performed to demonstrate its computational capabilities and superiorities in the metasurface design and analysis. The intrinsic dipole-based scattering mechanism of unit cell is confirmed. Compared to the HF and the HP, the DWS provides superior capability of computing the diffraction field within the paraxial and non-paraxial, near-field and far-field region generated by the metasurface and the

target field, and shows perfect consistency with the full-wave analysis and the theoretical results. It will greatly improve the creation accuracy and efficiency of the metasurface-based devices, especially for the near field or low frequency applications, and contribute to their rapid prototyping and further evolution.

However, it should be pointed out that the weak coupling among unit cells is not considered in the DWS method. The effect on the diffraction near-field including evanescent field or surface field of metasurfaces caused by this coupling would be non-negligible and in turn reduce the modeling and calculation accuracy of our proposed DWS. In plasmonic and all-dielectric metasurfaces, in addition to the electric, magnetic, or toroidal dipole resonances, high-order multipole resonances may also occur, especially in the deep-subwavelength near-field region. Therefore, in our future work, these high-order multipole resonances would also be taken into account and added to the fundamental dipole. These could effectively improve the calculation accuracy of our proposed method and extend its effective computational region to the deep-subwavelength near-field or even surface-field region of metasurfaces.

References

[1] H. T. Chen, A. J. Taylor, and N. Yu, "A review of metasurfaces: Physics and applications," *Rep. Prog. Phys.*, vol. 79, no. 7, 2016, Art. no. 076401.

[2] D. C. Wang *et al.*, "Multiband switchable terahertz quarter-wave plates via phase-change metasurfaces," *IEEE Photon. J.*, vol. 8, no. 1, Feb. 2016, Art. no. 5500308.

[3] F. Ding, A. Pors, and S. I. Bozhevolnyi, "Gradient metasurfaces: Fundamentals and applications," *Rep. Prog. Phys.*, vol. 81, no. 2, 2018, Art. no. 026401.

[4] Y. L. He *et al.*, "Order-controllable cylindrical vector vortex beam generation by using spatial light modulator and cascaded metasurfaces," *IEEE Photon. J.*, vol. 9, no. 5, Oct. 2017, Art. no. 6101710.

[5] M. Khorasaninejad and F. Capasso, "Metalenses: Versatile multifunctional photonic components," *Science*, vol. 358, no. 6367, 2017, Art. no. eaam8100.

[6] W. Wan, J. Gao, and X. Yang, "Metasurface holograms for holographic imaging," *Adv. Opt. Mater.*, vol. 5, no. 21, 2017, Art. no. 1700541.

[7] R. Dharmavarapu *et al.*, "MetaOptics: Opensource software for designing metasurface optical element GDSII layouts," *Opt. Express*, vol. 28, no. 3, pp. 3505–3516, 2020.

[8] N. Yu *et al.*, "Light propagation with phase discontinuities: Generalized laws of reflection and refraction," *Science*, vol. 334, no. 6054, pp. 333–337, 2011.

[9] F. Aieta *et al.*, "Out-of-plane reflection and refraction of light by anisotropic optical antenna metasurfaces with phase discontinuities," *Nano Lett.*, vol. 12, no. 3, pp. 1702–1706, 2012.

[10] H. Chu, J. Qi, S. Xiao, and J. Qiu, "A thin wideband high-spatial-resolution focusing metasurface for near-field passive millimeter-wave imaging," *Appl. Phys. Lett.*, vol. 112, no. 117, 2018, Art. no. 174101.

[11] Z. L. Deng *et al.*, "Facile metagrating holograms with broadband and extreme angle tolerance," *Light Sci. Appl.*, vol. 7, no. 78, pp. 1–8, 2018.

[12] Q. M. Chen *et al.*, "Wavelength and polarization multiplexed optical vortex demultiplexer," *J. Phys. D: Appl. Phys.*, vol. 52, no. 37, 2019, Art. no. 375104.

[13] D. Wen *et al.*, "Metasurface for characterization of the polarization state of light," *Opt. Express*, vol. 23, no. 8, pp. 10272–10281, 2015.

[14] K. Huang *et al.*, "Photon-nanosieve for ultrabroadband and large-angle-of-view holograms," *Laser Photon. Rev.*, vol. 11, no. 3, 2017, Art. no. 1700025.

[15] N. Estakhri, V. Neder, M. Knight, A. Polman, and A. Alu, "Visible light, wide-angle graded metasurface for back reflection," *ACS Photon.*, vol. 4, no. 2, pp. 228–235, 2017.

[16] S. A. Degtyarev, S. G. Volotovsky, and S. N. Khonina, "Sublinearly chirped metalenses for forming abruptly autofocusing cylindrically polarized beams," *J. Opt. Soc. Amer. B*, vol. 35, no. 8, pp. 1963–1969, 2018.

[17] M. Amin, O. Siddiqui, M. Farhat, and A. Khelif, "A perfect Fresnel acoustic reflector implemented by a Fano-resonant metascreen," *Appl. Phys. Lett.*, vol. 123, no. 14, 2018, Art. no. 144502.

[18] J. Zhao, H. Ye, K. Huang, Z. N. Chen, B. Li, and C. W. Qiu, "Manipulation of acoustic focusing with an active and configurable planar metasurface transducer," *Sci. Rep.*, vol. 4, no. 1, 2014, Art. no. 6257.

[19] B. Orazbayev, V. Pacheco-Peña, M. Beruete, and M. Navarro-Cía, "Exploiting the dispersion of the double-negative-index fishnet metamaterial to create a broadband low-profile metallic lens," *Opt. Express*, vol. 23, no. 7, pp. 8555–8564, 2015.

[20] Y. Cheng *et al.*, "Multi-polarization passive millimeter-wave imager and outdoor scene imaging analysis for remote sensing applications," *Opt. Express*, vol. 26, no. 16, pp. 20145–20159, 2018.

[21] Y. Meng *et al.*, "Passive millimeter wave imaging system based on helical scanning," *Sci. Rep.*, vol. 8, no. 1, 2018, Art. no. 7852.

[22] N. M. Caira and D. R. Smith, "Multispectral metasurface hologram at millimeter wavelengths," *Appl. Opt.*, vol. 57, no. 1, pp. A19–A25, 2018.

[23] Z. Wang *et al.*, "Huygens metasurface holograms with the modulation of focal energy distribution," *Adv. Opt. Mater.*, vol. 6, no. 12, 2018, Art. no. 1800121.
[24] A. Pan, M. Zhou, Y. Zhang, J. Min, M. Lei, and B. Yao, "Adaptive-window angular spectrum algorithm for near-field ptychography," *Opt. Commun.*, vol. 430, pp. 73–82, 2019.
[25] T. M. Bloomstein, M. F. Marchant, S. Deneault, D. E. Hardy, and M. Rothschild, "22-nm immersion interference lithography," *Opt. Express*, vol. 14, no. 14, pp. 6434–6443, 2006.
[26] P. Mehrotra, C. A. Mack, and R. J. Blaikie, "A solid immersion interference lithography system for imaging ultra-high numerical apertures with high-aspect ratios in photoresist using resonant enhancement from effective gain media," *Proc. SPIE*, vol. 8326, 2012, Art. no. 83260Z.
[27] H. Chu, J. Qi, R. Wang, and J. Qiu, "Generalized rayleigh-sommerfeld diffraction theory for metasurface-modulating paraxial and non-paraxial near-field pattern estimation," *IEEE Access*, vol. 7, pp. 57642–57650, 2019.
[28] Y. Z. Umul, "Modified diffraction theory of kirchhoff," *J. Opt. Soc. Amer. A Opt. Image Sci.*, vol. 25, no. 8, pp. 1850–1860, 2008.
[29] C. M. Roberts and V. A. Podolskiy, "Rigorous diffraction interface theory," *Appl. Phys. Lett.*, vol. 110, no. 17, pp. 1304–1307, 2017.
[30] K. Huang *et al.*, "Planar diffractive lenses: Fundamentals, functionalities, and applications," *Adv. Mater.*, vol. 30, no. 26, 2018, Art. no. 1704556.
[31] X. G. Luo, "Principles of electromagnetic waves in metasurfaces," *Sci. China Phys. Mech.*, vol. 58, no. 9, 2015, Art. no. 594201.
[32] K. Achouri and C. Caloz, "Design, concepts, and applications of electromagnetic metasurfaces," *Nanophotonics*, vol. 7, no. 6, pp. 1095–1116, 2018.